Application of an Efficient Rogowski Coil Sensor for Switch Fault Diagnosis and Capacitor ESR Monitoring in Nonisolated Single-Switch DC–DC Converters

Ebrahim Farjah, *Member, IEEE*, Hadi Givi, *Student Member, IEEE*, and Teymoor Ghanbari

***Abstract*—Power switches and electrolytic capacitors are the most vulnerable components in the power electronic converters. Any failure in these components may result in severe damages, if no remedial action is employed. Prior to any remedy, the first step is fault diagnosis. In this paper, a new type of Rogowski coil sensor is proposed. The sensor captures the inductor current derivative, which contains suitable signatures for switch fault diagnosis and capacitor lifetime monitoring in nonisolated single-switch dc–dc converters. Using the captured signal, detection of switch open-circuit and short-circuit faults is realized by a simple logic circuit. Furthermore, a new capacitor lifetime monitoring technique is proposed, which employs this signal for calculating equivalent series resistance of the capacitor. The proposed sensor has some remarkable advantages. Due to its nonmagnetic core, the problem related to nonlinear response of magnetic cores at high frequencies will not be encountered. Furthermore, the proposed cost-efficient approach can be easily implemented even for already fabricated converters. The performance of the proposed sensor is evaluated using some finite-element simulations and experiments for a buck converter. The results confirm the capabilities of the sensor for switch fault diagnosis and capacitor lifetime monitoring in nonisolated single-switch dc–dc converters.**

***Index Terms*—Capacitor lifetime monitoring, dc–dc converters, magnetic sensors, Rogowski coil (RC), switch fault diagnosis.**

I. Introduction

NOWADAYS, dc–dc switching converters are widely used in different applications, such as portable electronic devices, variable speed drives, flexible high-voltage direct-current systems, electric or hybrid electric vehicles, transmission systems, and renewable energy systems.

Since a failure in these converters may result in the malfunction of the whole system, their reliability is a great concern [1]. Consequently, a suitable monitoring and fault diagnosis system as well as an appropriate fault-tolerant strategy should be employed [2].

Manuscript received March 15, 2015; revised December 15, 2015 and February 17, 2016; accepted March 21, 2016. Date of publication April 7, 2016; date of current version November 11, 2016. Recommended for publication by Associate Editor T. M. Lebey.

E. Farjah and H. Givi are with the School of Electrical and Computer Engineering, Shiraz University, Shiraz 71847-64175 Iran (email: farjah@shirazu.ac.ir; hadi.givi@gmail.com).

T. Ghanbari is with the School of Advanced Technologies, Shiraz University, Shiraz 71847-64175 Iran (email: teymoor_ghanbari@yahoo.com)

Color versions of one or more of the figures in this paper are available online at http://ieeexplore.ieee.org.

Digital Object Identifier 10.1109/TPEL.2016.2552039

A stochastic analysis of the failures per component in commercial switch-mode power supplies is presented in [3]. According to this research, the electrolytic capacitors and power switches are the most vulnerable components, which are responsible for about 90% of the faults in these converters. Power switch failures are broadly classified into open-circuit fault (OCF) and short-circuit fault (SCF) [4]. On the other hand, capacitor faults are divided into structural and parametric failures [5].

Upon fault occurrence in any fault-tolerant system, the first step is fault diagnosis [6]. This step includes fault detection and identification, by which type and location of the fault are determined. In the next step, a suitable remedial strategy should be employed to isolate the faulty component and realize a fault-tolerant converter, which ensures safe and continuous operation of the system [2]. However, fault diagnosis may not be sufficient for some faults such as inverter leg cross conduction and SCF of the freewheeling diode in dc–dc converters. Fault prognosis is necessary to protect the converters against these faults.

Many investigations have been directed to detect switch SCF and OCF for the converters, utilized in different applications such as power-electronic interface-based distributed generations and motor drives. The first step in any fault diagnosis technique is selection of suitable diagnosis criteria. The methods based on voltage or current signatures are attractive, since these signals are available using the already installed sensors. Therefore, output voltage and/or current (control variables) of the converter are utilized as the diagnosis criteria in many papers, which results in simple and low-cost methods [4], [7]–[9]. However, the control variables change slowly due to the output filter of the dc–dc converters, which leads to a considerable delay in the fault detection. Furthermore, the control variables may not contain enough signatures for accurate fault identification [10]. Some fault diagnosis techniques use a combination of the circuit signals as the diagnosis criteria. The dc-link current, the transformer primary voltage, and the switch gate driver signal have been combined for detection of the switch SCF in the phase-shifted full-bridge converters [11]. Besides, a remedial strategy has been presented to reconfigure these converters to an asymmetrical half-bridge converter in the postfault condition. In [12], some new methods have been proposed for fault detection and localization in grid-connected power converters including fault diagnosis for three-phase-uncontrolled rectifier, boost chopper, and inverter. A tolerant control has been proposed for switch

OCF in back-to-back and neutral-point-clamped (NPC) rectifiers for wind turbine generation systems in [13]. This approach is based on injection of the exact *d*-axis current value, which eliminates current distortion. An effective and robust algorithm has been proposed in [14] to detect the switch OCF in three-level NPC rectifiers, which employs the instantaneous voltage error. The switch SCF and OCF in buck converters or three-phase full-bridge inverters for brushless DC motor drivers are detected based on analysis of the faulty operating state in [15]. This method extracts the residual signals of the voltage observers and the measurements for fault detection. In [16], the cross correlation between the estimated and real currents is employed as a diagnosis criterion for switch OCF detection in a voltage-source inverter. Single switch and double switches OCFs have been detected for the voltage-source inverters by employing the concept of allelic points for the functions defined for three-phase currents [17]. In [18], some signal processing tools are applied on the measured current to detect simultaneous OCFs in an inverter-fed linear induction motor drive. To detect and identify the switch faults in switched-reluctance motor drives, an approach based on the difference between the amplitude of the measured current in normal and faulty conditions is presented in [19], which includes a tolerant scheme for postfault conditions. By inserting an auxiliary inverter leg, a fault-tolerant topology is presented in [20] for three-phase adjustable speed drives. In case of switch SCF and OCF, this auxiliary leg is utilized as a redundant leg. In [21], the switch SCF and OCF are discriminated from the healthy condition for a multilevel inverter (MLI) using multiresolution analysis. Upon fault occurrence in the MLI, the fault is detected through an analysis on the details of the wavelet transform (WT) levels. However, WT has some dramatic restrictions, in practice, such as measurement noise impact on its performance and requiring different sampling frequencies in the levels.

Different fault diagnosis criteria have been utilized in dc–dc converters including variations of the circuit variables [22], [23], the peak values of the dc-link current, the inductor current, and magnetic near field waveforms. In [22], slope of the inductor current is utilized as a criterion for switch fault diagnosis in nonisolated dc–dc converters, in which no additional sensor is required and the effects of disturbances are taken into account. A fault-tolerant three-level boost converter is proposed in [23] for photovoltaic applications. This scheme employs the control variables utilized for maximum power point tracking and dc-link capacitor voltage balance for switch OCF diagnosis. However, some components should be added to the original three-level boost converter to be reconfigured in postfault condition. For fault diagnosis in zero-voltage switching dc–dc converters, the peak values of the dc-link current pulse shapes have been analyzed in [24]. However, the required peak detector and integrator circuitry are relatively complex. The inductor current could also be utilized as a criterion for fault diagnosis. Using this signal and a field-programmable gate array tool, real-time detection of the switch OCF and SCF in single-switch dc–dc converters has been carried out [25]. Also, a redundant switch and a bidirectional switch are employed to reconfigure the converter after fault occurrence. In [26], shape of the inductor current is analyzed to achieve a fast fault diagnosis method for detection of switch OCF and SCF in dc–dc converters. Since the switching mode dc–dc converters are generally utilized at high frequencies, the Electromagnetic signals induced by the current and voltage variations also contain useful signatures for the diagnosis purpose [27], [28]. In [1], a systematical monitoring and diagnosis method is proposed for dc–dc converters using magnetic near-field waveforms. Although this method is applicable to different dc–dc converters, its calculations are complicated and the required magnetic probes are expensive. In [10], the voltage of the magnetic component captured by an auxiliary winding is utilized for switch fault diagnosis. Although this technique is simple, cost effective, and applicable for various dc–dc converters, adding an auxiliary winding for the measurement purpose has some restrictions due to nonlinear response of the core at high frequencies. Furthermore, this winding should be considered in design process of the converter and could not be utilized for already fabricated converters.

Electrolytic capacitors are widely used in power electronic converters due to their low cost, high density of energy, considerable value of capacitance, and voltage rating [29]. However, they may experience structural or parametric failures. In case of structural failures, the capacitor usually cannot be employed at all. Parametric failures refer to gradual degradation of the capacitor. These failures are more common and manifest themselves by increase in the capacitor equivalent series resistance (ESR) and/or decrease in its capacitance [5]. As a result, condition monitoring of these capacitors during operation is really essential [30], [31]. These capacitors are usually modeled as a capacitance in series with an ESR [30]–[32]. Due to ageing mechanism, value of the capacitance decreases, while the ESR increases. The increase in the ESR is more considerable and is the main criterion for capacitor condition monitoring. Typically, the capacitor end life is defined when the ESR value doubles in comparison with the initial value [33]. Many research has been published regarding the ESR calculation and estimation. The ESR calculation and estimation techniques can be classified into offline and online categories. Since the offline schemes require disconnection of the capacitor from the convertor, they are not preferred. However, they are inexpensive and easy to implement. In [31] and [32], high-precision *LCR* meters are utilized for measurement of the ESR. The online techniques have been interested since there is no need to disconnect the capacitor from the circuit for ESR measurement [5], [29], [34]–[39]. A simple relationship between the input current and the output voltage ripple has been used to estimate the ESR in [5]. In [29], the ESR is calculated by a digital filter using an injected ac current and the relevant output voltage ripple, considering temperature effect on the resistance. In [34] and [35], a ratio of the capacitor voltage to the supply voltage (square or sinusoidal) with a reference resistor is utilized to compute the ESR. However, the precision of this technique is highly dependent on the reference resistor error. The ESR could be estimated using the capacitor voltage, current ripple, and the load current [36]. In [37], a noninvasive online technique has been proposed to identify the capacitor equivalent circuit parameters for a buck converter, which needs no current sensor. In this technique, the

pulse-width-modulation signal and the output voltage are utilized to calculate the capacitor ESR and capacitance. For the induction machine drives, a novel approach has been proposed in [38] to estimate the capacitance value based on injection of a regulated ac component into the stator winding, while the motor is working in the regenerative mode. The injected signal leads to an ac component in the dc-link voltage and current, which could be utilized for capacitance estimation through a recursive least-square algorithm. In [39], the ratio between the measured ESR for a degraded capacitor and the expected ESR for a new capacitor at the same operating temperature is employed as an index to estimate the ESR of the aluminum electrolytic capacitors. Since this index is independent of the measurement temperature, it is suitable for degradation prognosis in automotive drive applications.

Rogowski coils (RCs) have outstanding specifications in comparison with other magnetic sensors such as linear response for wide range of frequency, low cost, high accuracy, and reliability. RCs are applied in various electrical systems for measurement [40]–[45].

In this paper, a new type of RC sensor (RCS) is proposed to realize switch fault diagnosis and capacitor lifetime monitoring in nonisolated single-switch dc–dc converters. The proposed sensor has some interesting advantages such as linear response for wide range of frequency, low cost, and simple implementation even for already fabricated converters. Using the RCS output, the diagnosis technique presented in [10] has been developed for detection of switch faults. The RCS output and the gate driver signal are employed to generate the required signals for switch OCF and SCF detection through a simple logic circuit. Moreover, a new capacitor lifetime monitoring technique is presented which employs the RCS output voltage for calculation of the capacitor ESR. The performance of the proposed method is evaluated using some simulations and experiments for a buck converter. The results confirm that switch fault diagnosis and capacitor ESR monitoring could be realized by the proposed sensor effectively.

The rest of this paper is organized as follows. Section II presents the operational principle and equivalent circuit model of a RC as well as the procedure for identification of the RC parameters. In Section III, the structure of the proposed RCS is introduced. Section IV deals with description of the switch fault diagnosis technique. The superiority of the RCS over the auxiliary winding proposed in [10] is discussed in Section V. In Section VI, a new technique for capacitor ESR monitoring is presented using the RCS output. The performance of the proposed sensor is evaluated using some finite-element simulations and experiments for a buck converter in Sections VII and VIII, respectively. Finally, the main results are concluded in Section IX.

II. Operating Principle and Equivalent Circuit Model of a RC

A. Operating Principle

The operating principle of a RC is like a current transformer except that its core is not magnetic. Its performance can be described using the Ampere and Faraday laws

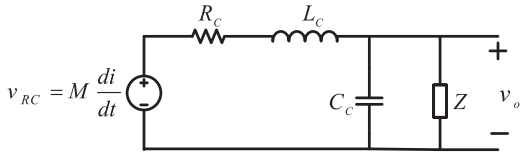

Fig. 1. Equivalent circuit model of a RC.

$$\begin{cases} i = \oint \overrightarrow{H}.\overrightarrow{dl} \\ \overrightarrow{B} = \mu_0 \overrightarrow{H} \\ \varphi = \iint_S \overrightarrow{B}.\overrightarrow{dS} \end{cases} \tag{1}$$

In (1), i, $\overrightarrow{H}$, $\overrightarrow{B}$, and μ_0 are the current enclosed by the coil, the magnetic field intensity, the magnetic flux density, and the magnetic permeability of the air, respectively. Parameter $\overrightarrow{dl}$ is the element of the flux path length. For the length element $\overrightarrow{dl}$, the corresponding surface element is $\overrightarrow{dS}$. The corresponding flux linkage is $d\varphi$. The output voltage of the coil is proportional to the rate of the flux change. Hence, using the Faraday law, the voltage relevant to $\overrightarrow{dl}$ can be expressed as

$$\begin{aligned} & v_{dl} = -\frac{d\varphi}{dt} = -\frac{d}{dt}\left(\iint_S \overrightarrow{B}.\overrightarrow{dS}\right) \\ & \Rightarrow v_{dl} = -\frac{d}{dt}\left(\iint_S \mu_0 \overrightarrow{H}.\overrightarrow{dS}\right) = -\mu_0 A \frac{dH}{dt}\cos\alpha. \end{aligned} \tag{2}$$

In (2), A is the turn area. The parameter α denotes the angle between $\overrightarrow{B}$ and $\overrightarrow{dS}$ vectors. Considering n as the number of turns and l as the length of the flux path, the induced voltage in the coil v_{RC} is

$$\begin{aligned} & v_{\mathrm{RC}} = \int_0^l v_{dl} n dl = -\mu_0 An \int_0^l \frac{dH}{dt}\cos\alpha \, dl \\ & \Rightarrow v_{\mathrm{RC}} = -\mu_0 An \frac{d}{dt}\int_0^l H\cos\alpha dl = -\mu_0 An \frac{di}{dt}. \end{aligned} \tag{3}$$

As expressed in (3), the output voltage of the coil is proportional to the derivative of the current enclosed by the coil. The mutual inductance is M

$$v_{\mathrm{RC}} = -M\frac{di}{dt}, \; M = \mu_0 An. \tag{4}$$

B. RC Equivalent Circuit Model and Parameters Identification

The equivalent circuit model of a RC is illustrated in Fig. 1. R_C, L_C, and C_C are the coil resistance, inductance, and capacitance, respectively. The parameters Z and v_o are the measurement impedance and the measured output voltage, respectively. As a result, the transfer function of the circuit can be expressed as

$$\frac{v_o}{v_{\mathrm{RC}}} = \frac{Z}{L_C Z C_C s^2 + (L_C + R_C Z C_C)\, s + R_C + Z}. \tag{5}$$

To identify the parameters of the RC equivalent circuit, a simple technique presented in [46] is utilized. This technique is based on the resonance frequency which reflects the magnetic

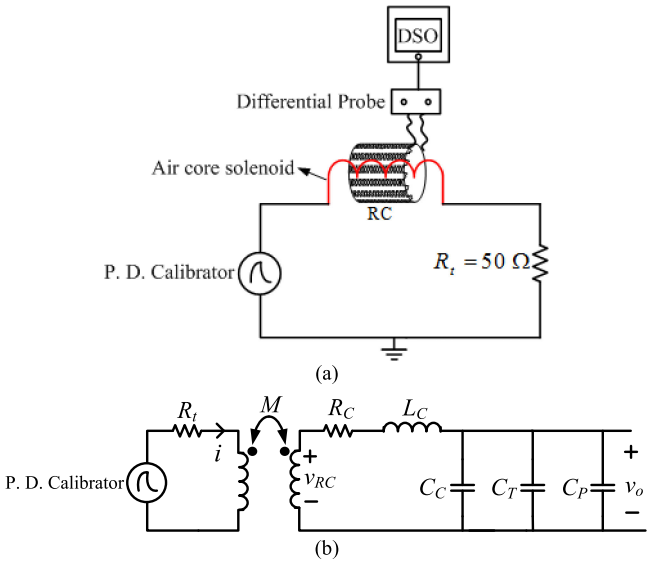

Fig. 2. RC parameters identification: (a) Circuit employed for parameters identification; and (b) detailed circuit diagram.

components of an induction sensor. The circuit employed for determination of the RC parameters is illustrated in Fig. 2(a). As shown in this figure, the partial-discharge calibrator (P. D. calibrator) injects a pulse into the circuit and the RC is installed on an air-core solenoid which is connected in series with a terminating resistor $R_t = 50\ \Omega$. This resistor is utilized to achieve a proper damping for the RC output [46]. The RC response is monitored using a digital storage oscilloscope (DSO). The detailed circuit diagram is shown in Fig. 2(b). The targeted parameters for identification are L_C and C_C. In Fig. 2(b), C_T is a test capacitor and C_P is the capacitance of the measurement probe.

Using the concept of resonance frequency, two sets of measurement are carried out to determine L_C and C_C. The first test is performed by connecting the test capacitor C_{T1} and the second test by connecting C_{T2}. The two resonance frequencies f_{11} and f_{12} are calculated by applying fast Fourier transform (FFT) on the coil output signals obtained from the mentioned tests. The resonance frequency can be expressed as

$$f = \frac{1}{2\pi\sqrt{L_C\left(C_C + C_P + C_T\right)}}. \tag{6}$$

The ratio of the two resonance frequencies results in

$$\begin{aligned} &\frac{f_{11}}{f_{12}} = \sqrt{\frac{C_C + C_P + C_{T2}}{C_C + C_P + C_{T1}}} \\ &\Rightarrow C_C + C_P + C_{T2} = \left(C_C + C_P + C_{T1}\right)\left(\frac{f_{11}}{f_{12}}\right)^2. \end{aligned} \tag{7}$$

Finally, it can be concluded that

$$C_C + C_P = \frac{C_{T1}\left(\frac{f_{11}}{f_{12}}\right)^2 - C_{T2}}{1 - \left(\frac{f_{11}}{f_{12}}\right)^2}. \tag{8}$$

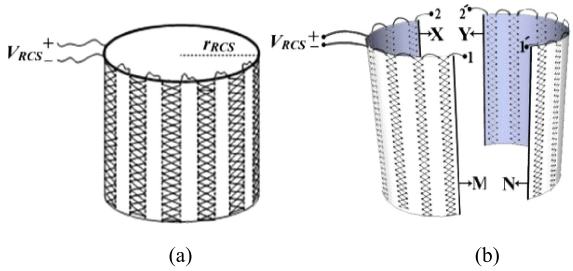

Fig. 3. Proposed RCS: (a) RCS with integrated core; and (b) RCS with split core.

Since C_P is known for the differential probe, C_C can be determined using (8). As a result, L_C is calculated by (6) through substituting f_{11} or f_{12}. A negligible difference appears in calculation of L_C by f_{11} and f_{12}. Hence, the average of the results can be used as the inductance of the coil

$$\begin{aligned} L_{C1} &= \frac{1}{2\pi\left(C_C + C_P + C_{T1}\right)f_{11}^2} \\ L_{C2} &= \frac{1}{2\pi\left(C_C + C_P + C_{T2}\right)f_{12}^2} \\ L_C &= \frac{L_{C1} + L_{C2}}{2}. \end{aligned} \tag{9}$$

III. Structure of the Proposed RCS

The structure of the proposed RCS is represented in Fig. 3. The RCS core is made up of nonmagnetic materials like Teflon. As seen in Fig. 3(a), the core is an integrated cylindrical shell because the RCS has been designed to be located on a cylindrical inductor, which is a finite solenoid. The RCS winding is composed of some parallel vertical lines of winding. These lines are uniformly distributed around the core. Each line includes a certain number of turns according to geometrical and electrical design considerations. The parallel vertical lines are connected in series so that the total voltage at the RSC terminals would be the summation of the induced voltages. The radius of the RCS core r_{RCS} should be selected as small as possible to minimize the distance between the sensor and the inductor. This would increase the amplitude of the induced voltage in the RCS winding as will be confirmed in Section VII.

Due to vertical structure of the RCS winding, it can be fabricated as a split core type instead of an integrated core straightforwardly. Fig. 3(b) shows the sensor with a split core in which the core is composed of two half cylindrical shells. In Fig. 3(b), the terminals 1 to 1′ and 2 to 2′ should be connected to sum the induced voltages of the two parts. Using such split core sensor, one can utilize the sensor for any already fabricated inductor with different shapes. Several different split core RCS have been presented by now. However, the proposed RCS is a novel structure. In fact, the main novelty of this split core RCS is relevant to design of a suitable structure by which the main portion of the linkage flux of the converter inductor can be monitored.

As shown in Fig. 3, one can observe that both integrated and split core structures have the same specifications.

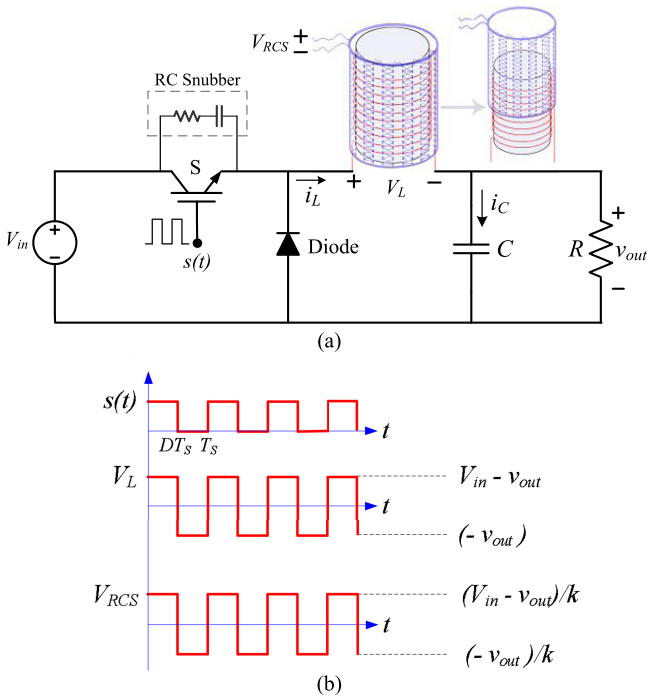

Fig. 4. Buck converter: (a) Circuit diagram with the RCS; and (b) gate signal, inductor voltage, and the RCS output voltage for normal condition.

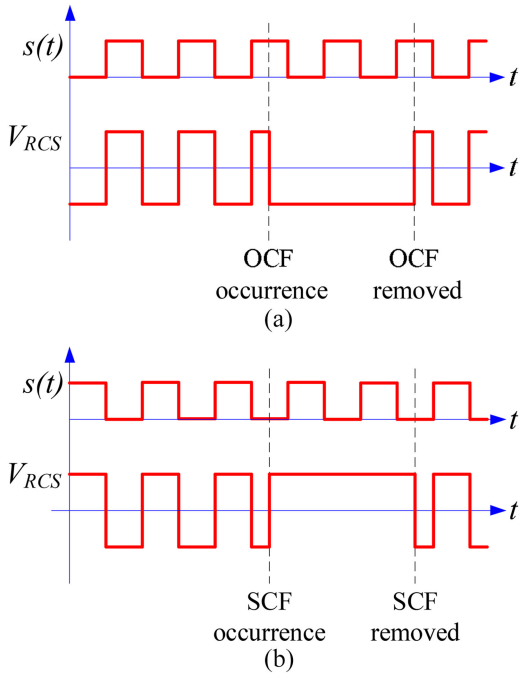

Fig. 5. Gate signal and the RCS output voltage in case of switch fault occurrence: (a) OCF; and (b) SCF.

In fact, when the two parts of the RCS with split core are installed around the converter inductor, their edges entitled (M, N) and (X, Y) in Fig. 3(b) are stuck together. Therefore, there is no difference in their equivalent circuits and the corresponding parameters R_C, L_C, and C_C.

The sensors illustrated in Fig. 3 are compact and cheap. They could be easily designed and implemented even for an already fabricated inductor. Furthermore, due to their nonmagnetic cores, they have linear response for a wide range of frequency. Hence, accurate and reliable measurements at high frequencies can be achieved by these sensors for switching-mode dc–dc converters.

IV. Description of the Switch Fault Diagnosis Technique

In this paper, the output of the RCS and the gate driver signal are utilized to diagnose the switch OCF and SCF in nonisolated single-switch dc–dc converters. The switch fault diagnosis technique will be explained for a buck converter. However, application of the technique for other nonisolated single-switch dc–dc converters is similar.

Fig. 4(a) shows a buck converter with the proposed RCS located on the inductor. In Fig. 4(a), *s(t)*, $V_{\rm RCS}, V_{\rm in}, v_{\rm out}, V_L, i_L$, and i_C denote the gate driver signal, the RCS voltage, input voltage, output voltage, inductor voltage, inductor current, and capacitor current, respectively. Parameters *L*, *C*, and *R* represent the buck converter inductor, capacitor, and load resistor, respectively. It is assumed that the converter operates in the continuous conduction mode.

Fig. 4(b) illustrates the signals *s(t)*, V_L, and $V_{\rm RCS}$ for the converter during normal operation. In Fig. 4(b), T_S and *D* are the period and duty cycle of *s(t)*, respectively. The parameter *k* represents the ratio between the inductor and the RCS voltages, $k = \frac{V_L}{V_{\rm RCS}} = \frac{L}{M}$ in which *M* is the RCS mutual inductance.

The voltage across the inductor and the RCS output voltage for normal operation of a buck converter could be expressed as

$$\begin{aligned} &\text{switch : off} \Rightarrow s(t) = 0 \Rightarrow V_L = -v_{\rm out} \\ &\Rightarrow V_L < 0 \Rightarrow V_{\rm RCS} = \frac{V_L}{k} < 0 \\ &\text{switch : on} \Rightarrow s(t) = 1 \Rightarrow V_L = V_{\rm in} - v_{\rm out} \\ &\Rightarrow V_L > 0 \Rightarrow V_{\rm RCS} = \frac{V_L}{k} > 0. \end{aligned} \tag{10}$$

As $V_{\rm in}$ is higher than $v_{\rm out}$, during normal operation of a buck converter, the RCS output voltage is positive and negative in case of switch-on and switch-off states, respectively, as shown in Fig. 4(b). This is true for other nonisolated single-switch dc–dc converters such as boost and buck–boost converters.

Unlike the normal condition, once a switch OCF occurs, $V_{\rm RCS}$ would be negative regardless of the gate signal status. On the other hand, in case of a switch SCF occurrence, $V_{\rm RCS}$ would be positive whether the gate signal is on or off. This concept is illustrated in Fig. 5 and is the basis of the fault diagnosis technique utilized in this paper. In Fig. 5, it is assumed that the switch is ideal and the output voltage does not change after fault occurrence.

According to Figs. 4(b) and 5, switch OCF can be detected when the gate signal is at the high level, while the occurrence of switch SCF could be identified when the gate signal is off. To realize fault diagnosis, the logic circuit proposed in [10] has

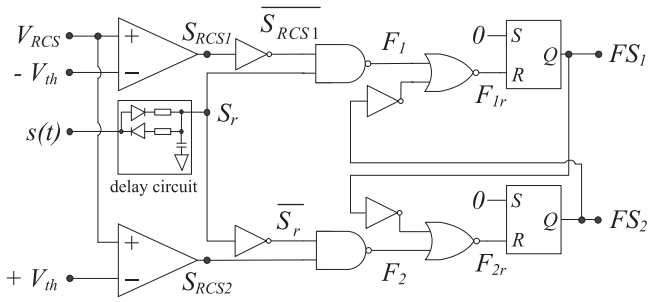

Fig. 6. Modified version of the fault diagnosis circuit proposed in [10].

TABLE I
VALUES OF THE LOGIC SIGNALS IN THE FAULT DIAGNOSIS CIRCUIT FOR DIFFERENT OPERATING CONDITIONS

Signal name	**Operating condition**					
	Normal		Switch OCF		Switch SCF	
	$s(t)=1$	$s(t)=0$	$s(t)=1$	$s(t)=0$	$s(t)=1$	$s(t)=0$
S_{RCS1}	1	0	0	0	1	1
S_{RCS2}	1	0	0	0	1	1
S_r	1	0	1	0	1	0
F_1	1	1	0	1	1	1
F_2	1	1	1	1	1	0
F_{1r}	0	0	1	0	0	0
F_{2r}	0	0	0	0	0	1
FS_1	1	1	**0**	1	1	1
FS_2	1	1	1	1	1	**0**

been modified in this paper as shown in Fig. 6. In Fig. 6, V_{th} is a threshold voltage which is a little higher than zero in the order of some millivolts. The output of the RCS is compared with $-V_{\mathrm{th}}$ and $+V_{\mathrm{th}}$ for generating S_{RCS1} and S_{RCS2}. As a result, when V_{RCS} is positive, the signals S_{RCS1} and S_{RCS2} are at the high level. Furthermore, for negative values of V_{RCS}, they become low. Detailed information about the signal values in the fault diagnosis circuit for different operating conditions is presented in Table I.

The initial values for the inputs of both reset-set flip flops are $S=1$, $R=0$. Hence, the Q outputs of the flip flops are at the high level in the initial state. Then, the S inputs of the flip flops are set to zero as depicted in Fig. 6 and the R ports are connected to F_{1r} and F_{2r}, respectively.

The signals FS_1 and FS_2 are both at the high level under normal condition because $F_{1r}=F_{2r}=0$. Once a switch OCF occurs, FS_1 becomes low while FS_2 remains at the high level. In case of a switch SCF, FS_2 becomes low and FS_1 remains at the high level. As a result, switch fault diagnosis of nonisolated single-switch dc–dc converters could be realized by monitoring FS_1 and FS_2 signals as bolded in the last two rows of Table I.

One important feature of this diagnosis technique is that its maximum delay for switch fault detection is less than one switching cycle (The propagation delay in logic gates is negligible in comparison to switching cycle). For the switch OCF condition, FS_1 becomes low for $s(t)=1$. Hence, the maximum OCF diagnosis delay is related to the occurrence of a switch OCF while $s(t)$ is in the beginning of its low-level interval. In this situation, the switch OCF would be diagnosed after $(1-D)\ T_{\mathrm{S}}$ because it could not be detected until $s(t)$ becomes high. In case of switch SCF occurrence, FS_2 becomes low for $s(t)=0$. The maximum SCF detection delay is related to the switch SCF occurrence when $s(t)$ is in the beginning of its high-level interval. In this case, the switch SCF would be detected after DT_S, when $s(t)$ becomes low.

For large values of D, DT_S which is the maximum delay of SCF detection tends to T_S. On the other hand, $(1-D)T_{\mathrm{S}}$ which is the maximum OCF detection delay tends to T_S for small values of D. As a result, the maximum delay for switch fault detection is less than one switching cycle.

In comparison to the logic circuit proposed in [10], two comparators are employed in Fig. 6. Furthermore, the negative outputs of the top and bottom comparators are set to $-V_{\mathrm{th}}$ and $+V_{\mathrm{th}}$, respectively. Using these modifications, the algorithm performance would be accurate for even large or small values of duty cycle as well as the converters with closed-loop control. The output of the RCS for a buck converter could be expressed as follows:

$$\begin{aligned}
&V_{\mathrm{RCS}} = M\tfrac{di_L}{dt}\\
&\text{switch : on} \Rightarrow V_{\mathrm{RCS}} = M \times \frac{V_{\mathrm{in}} - v_{\mathrm{out}}}{L}\\
&\Rightarrow V_{\mathrm{RCS}} = \frac{\mathrm{MV_{in}}}{L}(1-D)\\
&\text{switch : off} \Rightarrow V_{\mathrm{RCS}} = M \times \frac{(-v_{\mathrm{out}})}{L}\\
&\Rightarrow V_{\mathrm{RCS}} = \frac{-\mathrm{MV_{in}}}{L}D\\
&\Rightarrow V_{\mathrm{RCS}} = \begin{cases} \dfrac{\mathrm{MV_{in}}}{L}(1-D), \text{switch : on} \\ \dfrac{-\mathrm{MV_{in}}}{L}D, \text{switch : off} \end{cases}.
\end{aligned} \tag{11}$$

As a result, for large values of D, the amplitude of V_{RCS} is small for switch "on" intervals. On the other hand, the amplitude of the RCS voltage during switch "off" intervals would be small for small values of D. Both cases may lead to diagnosis mistake when comparing V_{RCS} with the threshold voltage, $V_{\mathrm{th}}=0$ in the logic circuit presented in [10]. As seen in Fig. 6, for generating FS_1 which is utilized for switch OCF detection, the RCS output is compared with $-V_{\mathrm{th}}$. Hence, for large values of D, although V_{RCS} is small during the switch "on" interval, it is compared with a small negative threshold which results in $S_{\mathrm{RCS1}}=1$. Since $s(t)=1$, in this interval, it results in $FS_1=1$ which informs normal condition. Similarly, for the converters with closed-loop control, the switch may be kept "on" for some switching periods ($D\approx 1$) to compensate step-load variations. In such condition, although the RCS output becomes zero, it is compared with a small negative value, and, hence, $S_{\mathrm{RCS1}}=1$. According to Table I, both FS_1 and FS_2 signals would be high indicating normal operation. In case of switch OCF, the RCS output is negative and as $V_{\mathrm{RCS}} < -V_{\mathrm{th}}$, $S_{\mathrm{RCS1}}=0$ which results in $FS_1=0$ for $s(t)=1$ as presented in Table I.

On the other hand, to generate FS_2 for switch SCF detection, $V_{\rm RCS}$ is compared with $+V_{\rm th}$. For small values of D, although $V_{\rm RCS}$ has a small negative amplitude during the switch "off" interval, it is compared with a small positive threshold which results in $S_{\rm RCS2} = 0$. Since $s(t) = 0$ in this interval, it leads to $FS_2 = 1$ based on Table I which indicates normal condition. In case of switch SCF occurrence, $V_{\rm RCS}$ remains positive and since it is compared with a small positive threshold, $S_{\rm RCS2} = 1$. As a result, FS_2 becomes low for $s(t) = 0$ and the SCF is diagnosed.

V. Superiority of the Proposed RCS Over the Auxiliary Winding in [10]

The proposed sensor has some superiority over the auxiliary winding proposed in [10], which are as follows.

1) The RCS can be utilized for already fabricated inductors straightforwardly, while implementation of the method presented in [10] may encounter some limitations in this case. Generally, the size of the inductor core is designed to be completely filled by the winding and adding an auxiliary winding to an already fabricated inductor, requires resizing of the inductor core. Furthermore, since the inductor winding is firmed by a special fluid, reusing the winding on a resized core has some limitations and even may be impossible.
   Based on the abovementioned discussion, using the proposed RCS instead of the auxiliary winding has evident economic justification in case of already fabricated inductors.
2) Ferrite cores are typically utilized for high-frequency magnetic devices. Due to low conductivity of the ferrites, it is possible to use large blocks of ferrite while maintaining low eddy-current losses. On the other hand, ferrites have a low-saturation flux density. Hence, relatively large ferrites should be used for power conversion purposes. This requirement for large-size core is in contrast with some of the assumptions considered in the design of high-frequency devices. In particular, the assumption of uniform distribution of the magnetic flux throughout the core cross section, and, therefore, uniform losses in the core. Furthermore, in order to have low eddy-current losses, the core should be small relative to the material skin depth. Both assumptions including uniform flux distribution and low eddy-current losses are challenged by the large ferrite cores required for high power conversion.
   Based on the aforementioned design considerations, resizing the inductor core to install the auxiliary winding leads to increase in the converter losses, especially in high-power and high-frequency applications. Therefore, the use of auxiliary winding results in the reduction of the converter efficiency, while adding the proposed sensor has not any negative impact on the converter efficiency.
3) Since the ferrite cores have different performances in various frequency bands, suitable selection of the inductor core for power conversion is an important key point. Such ferrite core may have unsuitable response for the measurement purpose. Consequently, a compromise should be carried out to find a suitable ferrite core for both power conversion and measurement purposes. Therefore, substituting the inductor core may be unavoidable. Thus, using a ferrite core with the mentioned specifications is not economic in comparison with employing the RCS.
4) The response of ferrite cores is linear in limited frequency ranges, while the RCS achieves linear response for an extensive frequency band due to its nonmagnetic core. Hence, the RCS is more accurate in comparison with the auxiliary winding for switch fault diagnosis.
5) In case of SCF in the converter, the magnetic core may be saturated. Consequently, the performance of the fault diagnosis techniques which are sensitive to core saturation may degrade, while the saturation problem will not be encountered for the RCS. As a result, application of the RCS improves the reliability of different diagnosis techniques, which use magnetic flux criteria for fault detection and identification.

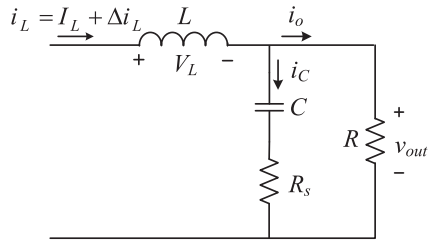

Fig. 7. Buck converter output considering the capacitor ESR.

VI. Application of the RCS for Capacitor Lifetime Monitoring

In this section, the output of the RCS is employed for capacitor lifetime monitoring in nonisolated single-switch dc–dc converters. One efficient criterion for inspecting the capacitor lifetime is ESR. According to [5], a real electrolytic capacitor could be modeled by an ideal capacitor connected in series with ESR and the equivalent series inductance (ESL). On the other hand, the effect of ESL is not significant for typical switching frequencies [48]. As a result, the buck converter output considering the capacitor ESR is represented in Fig. 7.

As seen, the capacitor is modeled by an ideal capacitor in series with ESR. In Fig. 7, I_L, Δi_L, i_o, and R_s denote the dc component of the inductor current, the inductor current ripple, the load current, and the capacitor *ESR*, respectively. The dc component of the inductor current flows in the load, $i_o = I_L$. Since the amplitude of the load resistance is much larger than the impedance of the capacitor branch, the major portion of the inductor current ripple flows in the capacitor branch. In other words

$$R \gg \sqrt{\left(\frac{1}{\omega C}\right)^2 + R_s^2} \Rightarrow i_C \approx \Delta i_L. \tag{12}$$

On the other hand, the output voltage ripple can be expressed as

$$v_{\text{out}} = V_{\text{out}} + \Delta v_{\text{out}} = \underbrace{V_C + \Delta v_C}_{v_C} + \Delta v_{\text{ESR}}$$
$$\Rightarrow \Delta v_{\text{out}} = \Delta v_C + \Delta v_{\text{ESR}}. \quad (13)$$

In (13), V_{out} and Δv_{out} represent the dc component of the output voltage and the output voltage ripple, respectively. The parameters $v_C, V_C, \Delta v_C$, and Δv_{ESR} denote the capacitor voltage, the dc component of the capacitor voltage, the capacitor voltage ripple, and the ESR voltage ripple, respectively. Using (12) and (13), the capacitor ESR as a function of the output voltage ripple and the inductor current ripple is given as

$$\begin{cases} \Delta v_{\text{out}} = \Delta v_C + \Delta v_{ESR} \\ \Delta v_C = \frac{1}{C}\int (i_C)dt \\ \Delta v_{ESR} = R_s i_C \\ i_C \approx \Delta i_L \end{cases} \Rightarrow \Delta v_{\text{out}} \approx \frac{1}{C}\int (\Delta i_L)dt + R_s \Delta i_L$$
$$\Rightarrow R_s \approx \frac{\Delta v_{\text{out}} - \frac{1}{C}\int (\Delta i_L)dt}{\Delta i_L}. \quad (14)$$

The signals Δi_L and $\int (\Delta i_L)dt$ can be derived using the RCS output voltage

$$V_{\text{RCS}} = M\frac{di_L}{dt} \Rightarrow \begin{cases} \Delta i_L = \dfrac{1}{M}\displaystyle\int V_{\text{RCS}}dt \\ \displaystyle\int \Delta i_L\, dt = \int \left(\frac{1}{M}\int V_{\text{RCS}}dt\right) dt \end{cases}. \quad (15)$$

Accordingly, the capacitor ESR can be calculated using the output voltage ripple and the RCS output based on (14) and (15):

$$R_s \approx \frac{\Delta v_{\text{out}} - \frac{1}{MC}\int \left(\int (V_{\text{RCS}})\, dt\right) dt}{\frac{1}{M}\int (V_{\text{RCS}})\, dt}. \quad (16)$$

Generally, there is an already installed voltage sensor in the output of the converters by which one can extract Δv_{out}. Therefore, only the proposed sensor is sufficient for calculation of the ESR by (16).

Three important factors that affect the ESR value considerably are temperature, frequency, and ageing. The ESR of an aluminum electrolytic capacitor increases as a result of temperature or frequency decrease [39]. Moreover, the capacitor ESR increases due to ageing mechanism. In fact, the effect of the mentioned factors on the ESR should be considered to monitor the capacitor lifetime accurately. The impact of temperature and frequency variations as well as ageing on the proposed ESR calculation technique is evaluated in Section VIII-C.

VII. Finite-Element Simulation Results

The operating principle of the proposed RCS is based on magnetic induction. On the other hand, extracting the magnetic flux expressions for outside of a finite solenoid is so complex and requires several approximations [47]. Hence, application of numeric methods like finite-element method (FEM) is suitable in this case. The inductor of the dc–dc converter which is a finite solenoid and the proposed RCS are simulated using three-dimensional (3-D) FEM. Maxwell software is utilized for FEM analysis.

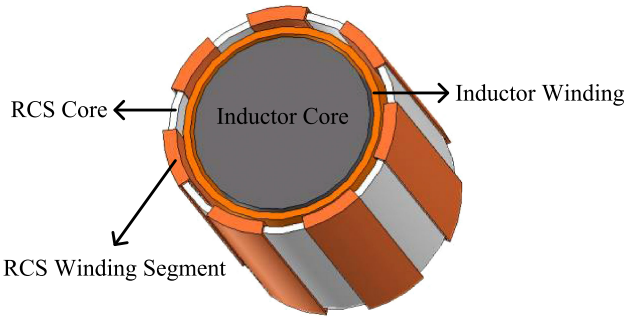

Fig. 8. Finite-element 3-D model of the inductor and RCS.

TABLE II
Specifications of the FEM Simulation

Parameter	Value/specification
Inductor core radius	12 mm
Inductor core height	30 mm
RCS core inner radius	14.5 mm
RCS core outer radius	15.5 mm
RCS core height	30 mm
Number of RCS winding turns	70
Inductor core material	M19_24G
RCS core material	Teflon

TABLE III
Specifications of the Buck Converter

Parameter	Value/Part Number
V_{in}	10
Duty cycle (D)	0.5
Power switch	IRF740
L	83 μH
C	470 μF, 63 V
R	5 Ω
Switching frequency (f)	50 kHz

Fig. 8 illustrates the 3-D model of the converter inductor and the RCS in Maxwell software. The simulation specifications are presented in Table II. As seen in Fig. 8, the RCS winding is composed of seven segments, each containing ten turns. These segments are connected in series to achieve 70 turns for the RCS. The segments are connected in series in a way that the RCS terminal voltage would be summation of the segment voltages.

The buck converter is considered for simulations in this section. However, the operating principles are the same for other nonisolated single-switch dc–dc converters.

A buck converter with the parameters presented in Table III has been simulated in ORCAD software. Then, the inductor current waveforms for normal condition, switch OCF, and SCF occurrences are derived using ORCAD simulations. These currents are injected into the inductor of the finite-element 3-D model in Fig. 8. The RCS in Fig. 8 is open-circuited to evaluate

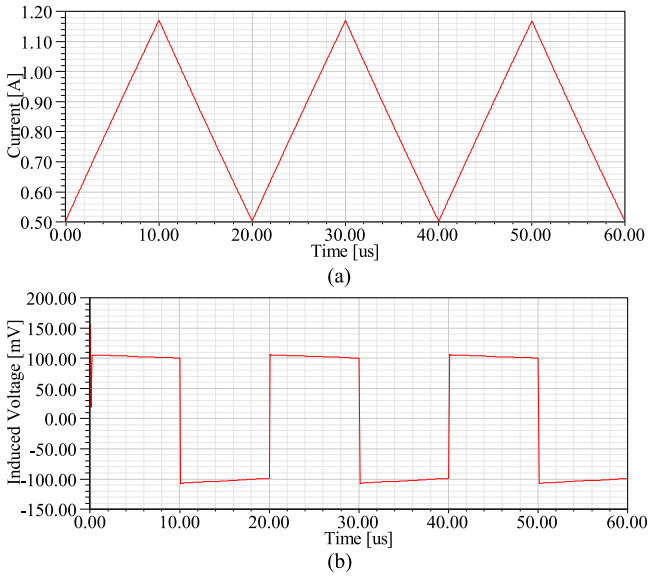

Fig. 9. Normal operation of the buck converter: (a) Inductor current; and (b) RCS induced voltage.

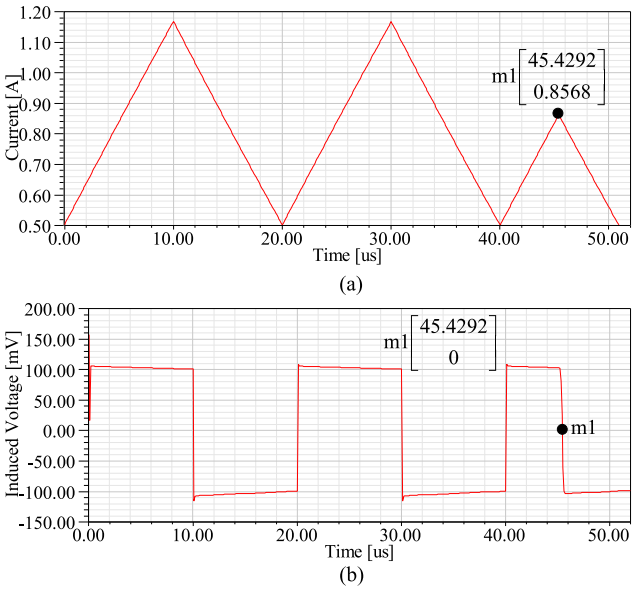

Fig. 11. Switch OCF occurrence in the buck converter: (a) Inductor current; and (b) RCS induced voltage.

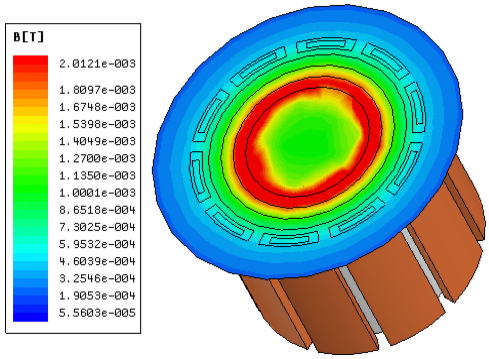

Fig. 10. Magnetic flux density distribution on a surface tangent to the RCS upper surface at $t = 5$ μs for the normal condition.

its induced voltage. Using FEM simulations, the voltage induced in the RCS would be analyzed for three conditions: normal condition, switch OCF occurrence, and switch SCF condition.

A. Normal Condition

Fig. 9(a) shows the steady-state current of the inductor of the buck converter during normal condition. This current is injected into the inductor in Fig. 8. The voltage induced in the RCS is illustrated in Fig. 9(b). The RCS voltage is proportional to the inductor current derivative. Hence, when the inductor current in Fig. 9(a) is rising, the RCS voltage is positive in Fig. 9(b) and for the intervals that the inductor current is decreasing, the RCS voltage is negative.

Fig. 10 represents the magnetic flux density distribution at $t = 5$ μs on a circular surface which is tangent to the RCS upper surface. It can be observed that at the vicinity of the inductor winding, the flux density is more than other regions and the flux density decreases as the distance from the inductor increases. Therefore, the RCS inner radius should be as small as possible to minimize its distance from the inductor and to increase the magnetic coupling between them.

B. Switch OCF Occurrence

In Fig. 11, it is assumed that the buck converter operates in the normal condition. Then, at $t = 45.4292$ μs, switch OCF occurs as denoted by m_1 in Fig. 11(a). Before m_1, the inductor current was increasing. After m_1, it starts to decrease due to switch OCF occurrence. The RCS voltage in Fig. 11(b) is positive between $t = 40$ μs and m_1. However, it becomes negative after m_1 as a result of the switch OCF, which can be utilized as the diagnosis criterion.

C. Switch SCF Occurrence

In Fig. 12(a), the buck converter operates in the normal condition till $t = 55.6365$ μs as specified by m_1. At m_1, the switch SCF occurs and the inductor current that was decreasing before m_1 starts to increase. The RCS voltage in Fig. 12(b) is negative before m_1, but becomes positive after m_1 due to switch SCF occurrence. This signature can be utilized as the criterion for switch SCF detection.

VIII. Experimental Results

In this section, the equivalent circuit parameters of the proposed sensor are extracted. Then, application of the sensor for switch fault diagnosis and capacitor lifetime monitoring in a typical dc–dc converter is discussed in detail.

A. Determination of the RCS Parameters and Frequency Response

Fig. 13(a) illustrates the experimental test bench employed for RCS parameters identification. The pulse generated by the P. D.

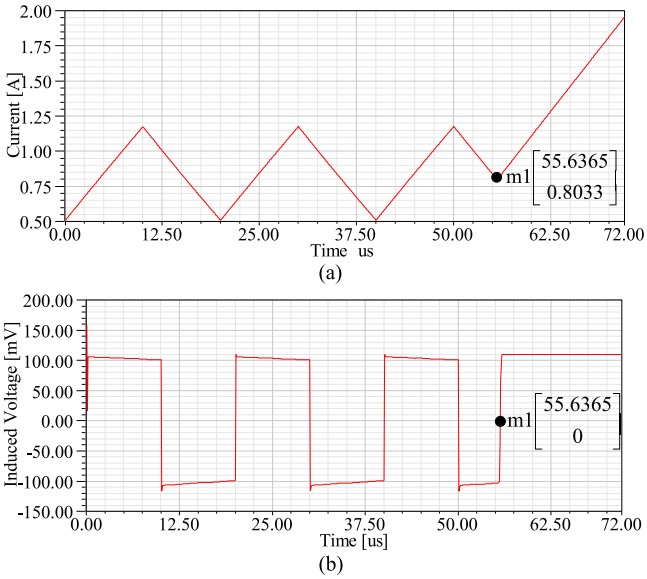

Fig. 12. Switch SCF occurrence in the buck converter: (a) Inductor current; and (b) RCS induced voltage.

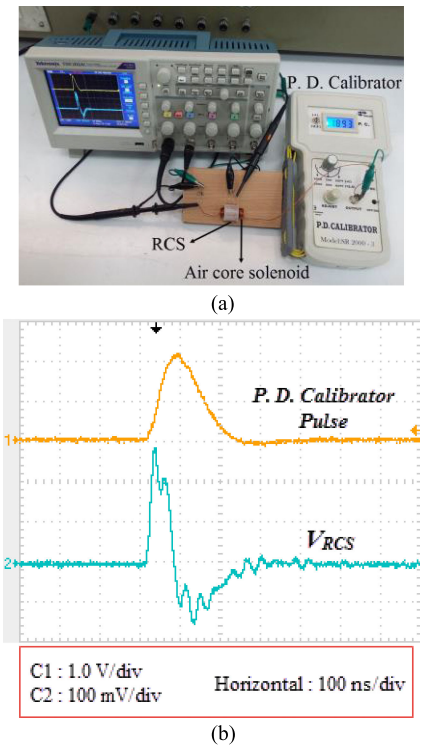

Fig. 13. Determination of the RCS parameters: (a) Employed test bench; and (b) experimental results, C1: P. D. calibrator pulse, C2: RCS output voltage.

calibrator and the RCS output voltage are shown in Fig. 13(b). In this section, the DSO is Tektronix TDS 2024C and the differential probe capacitance is $C_P = 20$ pF.

According to the method described in Section II-B, two tests should be carried out by connecting two different test capacitors across the RCS terminals. In this paper, the test capacitors are $C_{T1} = 220$ pF and $C_{T2} = 3.3$ nF. Using MATLAB software,

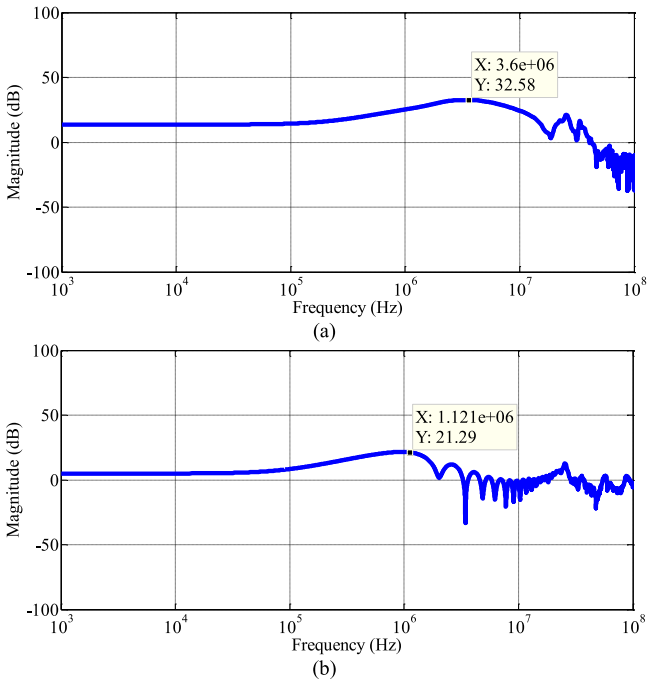

Fig. 14. FFT of the RCS response in experimental tests: (a) For $C_{T1} = 220$ pF; and (b) for $C_{T2} = 3.3$ nF.

the FFT of the RCS responses for these two tests are represented in Fig. 14(a) and (b), respectively. As seen in Fig. 14, the resonance frequencies for the mentioned tests are $f_{11} = 3.6$ MHz and $f_{12} = 1.121$ MHz, respectively. As expected, increase of the test capacitor results in the reduction of the resonance frequency.

Using (8), the RCS capacitance is calculated as

$$C_C + C_P = \frac{220\times10^{-12}\times\left(\frac{3.6}{1.121}\right)^2 - 3.3\times10^{-9}}{1-\left(\frac{3.6}{1.121}\right)^2} = 110.71\text{pF} \xrightarrow{C_p = 20\text{ pF}} C_C = 90.71\text{pF}. \quad (17)$$

The RCS inductance could be determined by (9). Consequently

$$\begin{cases} L_{C1} = 37.134\mu\text{H} \\ L_{C2} = 37.133\mu\text{H} \end{cases} \Rightarrow L_C = 37.13\mu\text{H}. \quad (18)$$

The RCS resistance R_C could be calculated by $R_C = \frac{\rho l_W}{A_W}$, in which ρ, l_W, and A_W are the resistivity, length, and cross section of the RCS winding, respectively. In case of employing the RCS for high-frequency applications, skin effect should be considered for determination of R_C.

Accordingly, the equivalent circuit parameters of the proposed RCS are listed in Table IV.

The oscilloscope input impedance (Z) is 1 MΩ. Consequently, using the RC transfer function expressed in (5) and the RCS parameters in Table IV, the Bode diagram of the proposed RCS is presented in Fig. 15.

According to Fig. 15, the response of the RCS is linear in a wide frequency range up to about 2.74 MHz. For any other design specifications of the RCS, the mentioned experimental

TABLE IV
RCS EQUIVALENT CIRCUIT PARAMETERS

Parameter	value
R_C	1.1 Ω
M	1.992 μH
C_C	90.71 pF
L_C	37.13 μH

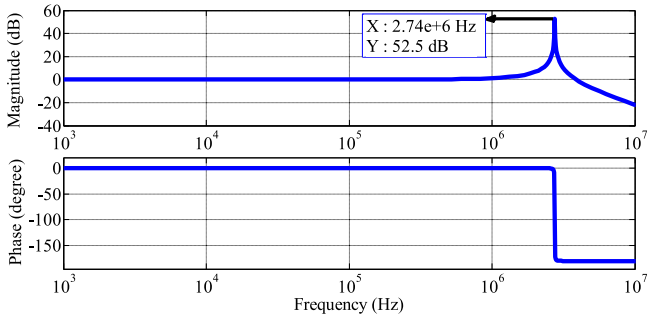

Fig. 15. Bode diagram of the proposed RCS.

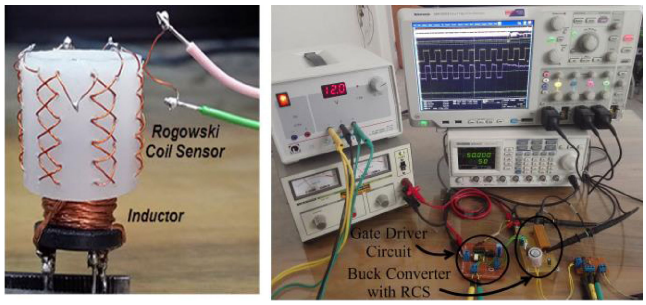

(a) (b)

Fig. 16. (a) Inductor and the RCS; and (b) employed test bench for evaluating the capability of the RCS.

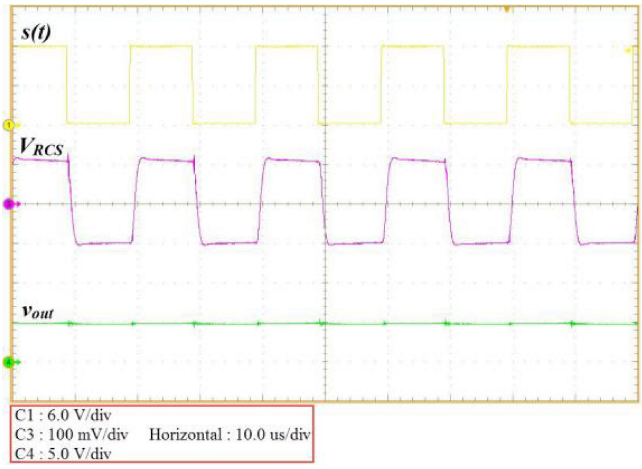

(a)

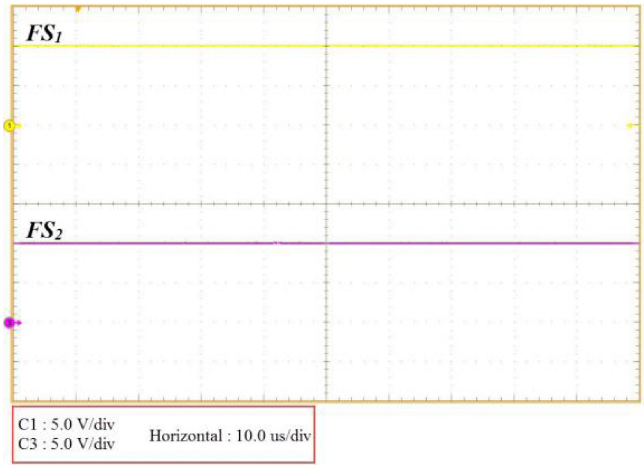

(b)

Fig. 17. Buck converter during normal operation: (a) C1: gate signal, C3: RCS voltage, C4: output voltage; and (b) outputs of the fault diagnosis circuit, C1: FS_1, C3: FS_2.

tests could be carried out to determine the relevant equivalent circuit parameters. Using the RCS transfer function in (5), its frequency response in the form of Bode diagram can be obtained.

B. Switch Fault Diagnosis Using RCS

In this section, the capability of the proposed RCS for switch fault diagnosis is verified. The RCS is implemented for a solenoid type inductor of a buck converter. The RCS and the employed test bench are depicted in Fig. 16. The specifications of the RCS and the buck converter are the same in Tables II and III, respectively.

Three cases are considered including normal operation, switch OCF, and switch SCF conditions. The gate driver signal, RSC output, output voltage, FS_1, and FS_2 are captured using digital oscilloscopes (Tektronix MSO5054). The logic circuit in Fig. 6 is implemented using DS1104 board.

1) Normal Condition: Fig. 17(a) shows the gate driver signal, RCS voltage, and the output voltage for normal operation of the buck converter. As discussed in Section IV, it is observed that $V_{\rm RCS}$ is positive for $s(t) = 1$, while it is negative for $s(t) = 0$. The outputs of the logic circuit are depicted in Fig. 17(b), where both FS_1 and FS_2 are at the high level for the normal condition.

According to Fig. 17(a), the absolute value of the RCS output voltage is $|V_{\rm RCS}| \approx 120{\rm mV}$, which is in good agreement with the simulation results in Fig. 9(b) and validates the simulations. Using the buck converter circuit equations, the mutual inductance of the RCS could be determined as

$$\begin{cases} V_{\rm out} = DV_{\rm in} = 0.5 \times 10 = 5{\rm V} \\ s(t) = 1 \Rightarrow V_L = V_{\rm in} - V_{\rm out} = L\frac{di_L}{dt} \\ |V_{\rm RCS}| = \left|M\frac{di_L}{dt}\right| \approx 0.12{\rm V}. \end{cases} \Rightarrow M = \frac{|V_{\rm RCS}|}{\left|\frac{di_L}{dt}\right|} \approx 1.992\mu{\rm H} \tag{19}$$

2) Switch OCF Occurrence: In this section, switch OCF occurrence is emulated using an auxiliary switch called "fault simulator switch," which is connected in series with the main switch of the buck converter. The gate signal of the fault simulator switch is denoted by *foc(t)*. During normal condition of the buck converter, $f_{OC}(t) = 1$ and the fault simulator switch is on. To emulate the switch OCF occurrence, the fault simulator

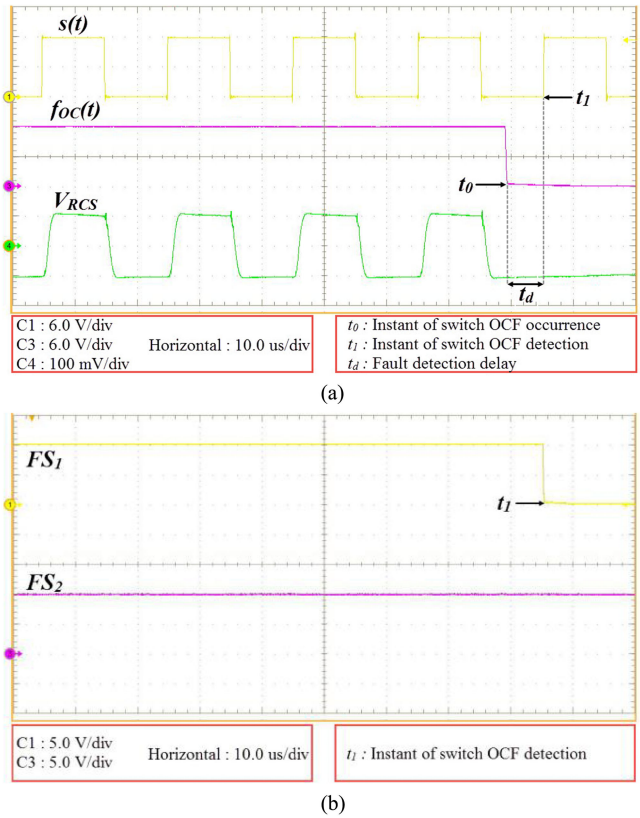

Fig. 18. Buck converter in case of switch OCF occurrence: (a) C1: gate signal of the main switch, C3: gate signal of the fault simulator switch, C4: RCS voltage; and (b) outputs of the fault diagnosis circuit, C1: FS_1, C3: FS_2.

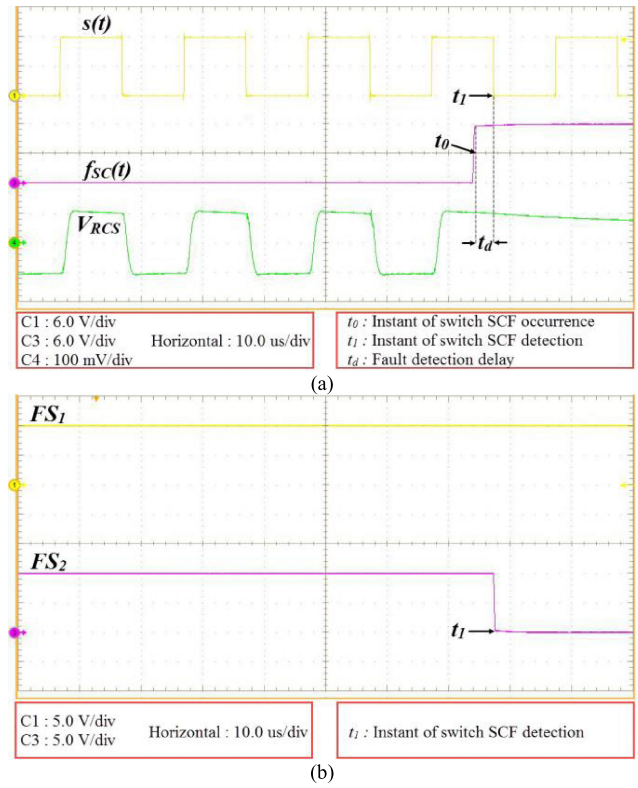

Fig. 19. Buck converter in case of switch SCF occurrence: (a) C1: gate signal of the main switch, C3: gate signal of the fault simulator switch, C4: RCS voltage; and (b) outputs of the fault diagnosis circuit, C1: FS_1, C3: FS_2.

switch is turned-off by setting $f_{OC}(t) = 0$. Therefore, the main switch current becomes zero. As a result, power flow from the input source to the output is interrupted.

Fig. 18(a) shows the gate signal of the main switch *s(t)*, the gate signal of the fault simulator switch $f_{OC}(t)$, and $V_{\rm RCS}$ in case of switch OCF occurrence. During normal operation, $f_{OC}(t) = 1$ and the RCS voltage is positive for $s(t) = 1$ and negative for $s(t) = 0$. At instant t_0, the main switch OCF is emulated by setting $f_{OC}(t) = 0$. Hence, the RCS voltage remains negative after this instant as explained in Section IV. However, since *s(t)* is low at t_0, the switch OCF could not be detected until instant t_1 at which *s(t)* becomes high. As a result, the fault detection delay t_d would be t_1–t_0. Since $t_d < (1 - D)T_S$, the proposed algorithm is able to detect the switch OCF in less than one switching cycle. The output signals of the fault diagnosis circuit are depicted in Fig. 18(b). It is observed that FS_1 becomes low at t_1, while FS_2 remains at the high level. Hence, the switch OCF is detected by FS_1 at t_1.

3) Switch SCF Occurrence: To realize the main switch SCF, an auxiliary switch called "fault simulator switch" is connected in parallel with the main switch of the buck converter. The gate of the fault simulator switch is excited by the signal *fsc(t)*. During normal condition, $fsc(t) = 0$ and the main switch is controlled by *s(t)*. The main switch SCF is emulated by setting $fsc(t) = 1$ and turning on the fault simulator switch.

The signals *s(t)*, *fsc(t)*, and $V_{\rm RCS}$ in case of the main switch SCF are shown in Fig. 19(a). During normal condition, the buck converter operates by switching the main switch and the fault simulator switch is off. At instant t_0, the fault simulator switch is turned on by setting $fsc(t) = 1$. Therefore, $V_{\rm RCS}$ remains positive after t_0. As explained in Section IV, the proposed algorithm can detect the switch SCF when $s(t) = 0$. Since *s(t)* is high at t_0, the switch SCF would be detected at t_1 at which *s(t)* becomes low. The fault detection delay in this case is t_1–t_0, which is less than DT_S. Therefore, the switch SCF is also detected in less than one switching cycle using the proposed technique. The fault diagnosis signals for this case are represented in Fig. 19(b). As seen, FS_2 becomes low at t_1 indicating switch SCF occurrence, while FS_1 remains at the high level.

C. Capacitor ESR Monitoring Using RCS

In this section, the output of the RCS is utilized to calculate the ESR of an electrolytic capacitor in a buck converter.

The specifications of the buck converter are the same as presented in Table III except the switching frequency. Application of the proposed ESR monitoring technique for other nonisolated dc–dc converters is similar.

The ESR of the capacitor is calculated using the RCS output based on (16). DS1104 board is utilized to calculate the ESR. On the other hand, the ESR determined by this technique is compared with the ESR offline measurement carried out by MASTECH MS5308 LCR TESTER.

1) Evaluation of the Proposed Capacitor ESR Monitoring Technique: Fig. 20(a) illustrates the RCS voltage, scaled waveform of $\Delta v_{\rm out}$, and the calculated ESR for the buck converter at $f = 100$ kHz and the ambient temperature $T = 25$ °C. It should be noted that since the peak value of $\Delta v_{\rm out}$ is small, its waveform has been scaled using Tektronix MSO5054 math function and the waveform of $10 \times \Delta v_{\rm out}$ is illustrated in Fig. 20.

As seen in Fig. 20(a), the capacitor ESR value calculated by the proposed technique is $R_S = 0.031\Omega$. On the other hand, using the offline measurement for this capacitor at $f = 100$ kHz, $R_S = 0.033\ \Omega$. The negligible difference between these two values of ESR is mainly due to the approximation in (12) and the difference between the capacitor temperatures in the measurements. When the capacitor is operating in the circuit, its temperature is higher in comparison with the offline measurement. Higher measurement temperature results in lower ESR [41].

2) Effect of the Operating Frequency on the ESR: In order to analyze the effect of operating frequency on the proposed ESR monitoring technique, the ESR of the buck converter capacitor is measured at $f = 50$ kHz and $T = 25$ °C. The RCS voltage, the scaled waveform of $\Delta v_{\rm out}$, and the calculated ESR for this operating condition are illustrated in Fig. 20(b). It can be observed that the ESR is $R_S = 0.035\ \Omega$ under the mentioned operating condition, while the ESR value is $R_S = 0.031\ \Omega$ at $f = 100$ kHz and for the same ambient temperature according to Fig. 20(a). As expected, increase in the operating frequency results in the ESR decrease [41]. Furthermore, since the ESR value for $f = 50$ kHz is higher; it can be observed that the peak value of $\Delta v_{\rm out}$ scaled waveform in Fig. 20(b) is higher than the corresponding value in Fig. 20(a). In other words, the ESR increase leads to higher peak value for the output voltage ripple.

3) Effect of the Temperature on the ESR: As mentioned in Section VI, due to increase/decrease in the temperature, the ESR of an aluminum electrolytic capacitor decreases/increases. In this section, the converter is located in a temperature chamber in which the ambient temperature is $T = 40$ °C. The ESR of the capacitor at $f = 100$ kHz is calculated by the proposed technique and the related waveforms are represented in Fig. 20(c). According to Fig. 20(c), the calculated ESR is $R_S = 0.020\ \Omega$. In comparison to Fig. 20(a) in which $R_S = 0.031\ \Omega$, the switching frequency in this test is the same but the temperature is higher. This indicates that the measurement temperature affects the value of the calculated *E*SR, considerably. Furthermore, since the ESR value in Fig. 20(c) is less than Fig. 20(a), the peak value of the output voltage ripple is lower, which results in lower peak value for the scaled waveform of $\Delta v_{\rm out}$ in Fig. 20(c).

4) ESR Measurement for a Degraded Capacitor: The utilized capacitor for the buck converter has been submitted to very high temperature (about 200°C) for 3 h. As a result, the capacitor has been degraded. After cooling down to $T = 25$ °C, its ESR is calculated at $f = 100$ kHz and the related waveforms are presented in Fig. 20(d). According to Fig. 20(d), the ESR of the degraded capacitor is $R_S = 0.058\ \Omega$. It indicates that the ESR increases considerably due to degradation. Furthermore,

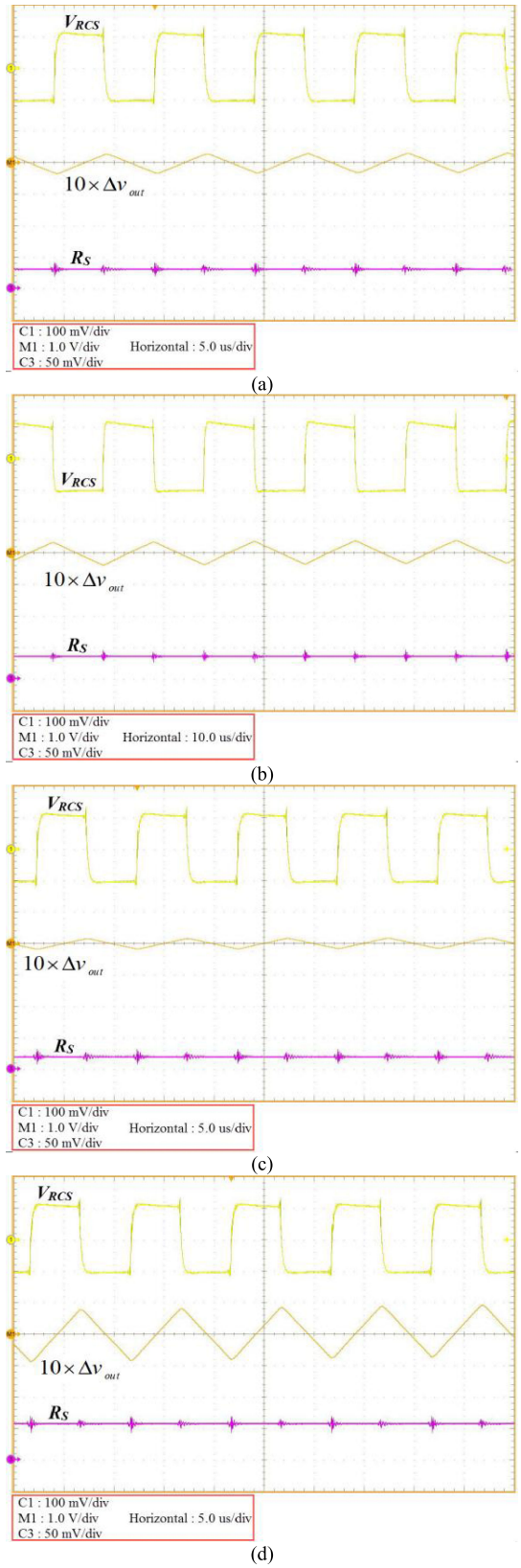

Fig. 20. Capacitor ESR monitoring using RCS; C1: RCS output voltage, M1: scaled waveform of the output voltage ripple ($10 \times \Delta v_{\rm out}$), C3: calculated ESR: (a) healthy capacitor at $f = 100$ kHz and $T = 25$ °C; (b) healthy capacitor at $f = 50$ kHz and $T = 25$ °C; (c) healthy capacitor at $f = 100$ kHz and $T = 40$ °C; and (d) degraded capacitor at $f = 100$ kHz and $T = 25$ °C.

in comparison with Fig. 20(a), the peak value of $\Delta v_{\rm out}$ scaled waveform in Fig. 20(d) is considerably higher. In fact, degradation of the capacitor leads to a noticeable increase in the ESR, which in turn results in higher peak value for the output voltage ripple.

IX. Conclusion

In this paper, application of a new type RCS is proposed for detection of switch OCF and SCF as well as capacitor ESR monitoring in nonisolated single-switch dc–dc converters. In comparison with the method, in which an auxiliary winding is employed to monitor the inductor flux, application of the RCS achieves several interesting advantages, such as low cost, compactness, linear response for a wide frequency range, higher accuracy, and reliability. The results obtained from the parameters identification test for the RCS confirm that the sensor has linear response in a wide frequency range up to about 2.74 MHz. Furthermore, it can be utilized even for already fabricated converters. Based on some finite-element simulations and experiments for a buck converter, it is confirmed that the RCS voltage could be utilized as an effective signature for switch fault diagnosis in nonisolated single-switch dc–dc converters. Using the RCS output and the gate driver signal, the switch OCF and SCF could be detected in less than one switching cycle. Furthermore, a new technique for capacitor lifetime monitoring is proposed, in which the RCS voltage is employed for calculating the capacitor ESR. The experimental results confirm the effectiveness of the proposed method for ESR monitoring in different operating conditions including variations of the temperature and frequency. As a result, the output of the proposed RCS can be utilized for both switch fault diagnosis and capacitor ESR monitoring.

Acknowledgment

The authors would like to thank Dr. M. Allahbakhshi and R. Khayam Hoseini for their cooperation in *RC* parameters identification tests.

References

[1] Y. Chen, X. Pei, S. Nie, and Y. Kang, "Monitoring and diagnosis for the DC–DC converter using the magnetic near field waveform," *IEEE Trans. Ind. Electron.*, vol. 58, no. 5, pp. 1634–1647, May 2011.

[2] B.-G. Park, K.-J. Lee, R.-Y. Kim, T.-S. Kim, J.-S. Ryu, and D.-S. Hyun, "Simple fault diagnosis based on operating characteristic of brushless direct-current motor drives," *IEEE Trans. Ind. Electron.*, vol. 58, no. 5, pp. 1586–1593, May 2011.

[3] A. Lahyani, P. Venet, G. Grellet, and P. Viverge, "Failure prediction of electrolytic capacitors during operating of a switch mode power supply," *IEEE Trans. Power Electron.*, vol. 13, no. 6, pp. 1199–1207, Nov. 1998.

[4] B. Lu and S. K. Sharma, "A literature review of IGBT fault diagnostic and protection methods for power inverters," *IEEE Trans. Ind. Appl.*, vol. 45, no. 5, pp. 1770–1777, Sep./Oct. 2009.

[5] A. M. R. Amaral and A. J. M. Cardoso, "On-line fault detection of aluminum electrolytic capacitors, in step-down DC-DC converters, using input current and output voltage ripple," *IET Power Electron.*, vol. 5, no. 3, pp. 315–322, Mar. 2012.

[6] Q. T. An, L. Z. Sun, K. Zhao, and L. Sun, "Switching function model based fast-diagnostic method of open-switch faults in inverters without sensors," *IEEE Trans. Power Electron.*, vol. 26, no. 1, pp. 119–126, Jan. 2011.

[7] R. Peuget, S. Courtine, and J. P. Rognon, "Fault detection and isolation on of a PWM inverter by knowledge-based model," *IEEE Trans. Ind. Appl.*, vol. 34, no. 6, pp. 1318–1326, Nov./Dec. 1998.

[8] K. Rothenhagen and F. W. Fuchs, "Performance of diagnosis methods for IGBT open circuit faults in voltage source rectifiers," in *Proc. IEEE Power Electron. Spec. Conf.*, 2004, pp. 4348–4354.

[9] W. Sleszynski, J. Nieznanski, and A. Cichowski, "Open-transistor fault diagnostics in voltage-source inverters by analyzing the load currents," *IEEE Trans. Ind. Electron.*, vol. 56, no. 11, pp. 4681–4688, Nov. 2009.

[10] S. Nie, X. Pei, Y. Chen, and Y. Kang, "Fault diagnosis of PWM DC–DC converters based on magnetic component voltages equation," *IEEE Trans. Power Electron.*, vol. 29, no. 9, pp. 4978–4988, Sep. 2014.

[11] X. Pei, S. Nie, and Y. Kang, "Switch short-circuit fault diagnosis and remedial strategy for full-bridge DC–DC converters," *IEEE Trans. Power Electron.*, vol. 30, no. 2, pp. 996–1004, Feb. 2015.

[12] T. Kamel, Y. Biletskiy, and L. Chang, "Fault diagnoses for industrial grid-connected converters in the power distribution systems," *IEEE Trans. Ind. Electron.*, vol. 62, no. 10, pp. 6496–6507, Oct. 2015.

[13] J.-S. Lee, K.-B. Lee, and F. Blaabjerg, "Open-switch fault detection method of a back-to-back converter using NPC topology for wind turbine systems," *IEEE Trans. Ind. Appl.*, vol. 51, no. 1, pp. 325–335, Jan./Feb. 2015.

[14] L. M. A. Caseiro and A. M. S. Mendes, "Real-time IGBT open-circuit fault diagnosis in three-level neutral-point-clamped voltage-source rectifiers based on instant voltage error," *IEEE Trans. Ind. Electron.*, vol. 62, no. 3, pp. 1669–1678, Mar. 2015.

[15] J. Fang, W. Li, H. Li, and X. Xu, "Online inverter fault diagnosis of buck-converter BLDC motor combinations," *IEEE Trans. Power Electron.*, vol. 30, no. 5, pp. 2674–2688, May 2015.

[16] M. Salehifar, R. Salehi Arashloo, M. Moreno-Eguilaz, V. Sala, and L. Romeral, "Observer-based open transistor fault diagnosis and fault-tolerant control of five-phase permanent magnet motor drive for application in electric vehicles," *IET Power Electron.*, vol. 8, no. 1, pp. 76–87, Jan. 2015.

[17] F. Wu and J. Zhao, "A real-time multiple open-circuit fault diagnosis method in voltage-source-inverter fed vector controlled drives," *IEEE Trans. Power Electron.*, vol. 31, no. 2, pp. 1425–1437, Feb. 2016.

[18] J.-H. Choi, S. Kim, D. S. Yoo, and K.-H. Kim, "A diagnostic method of simultaneous open-switch faults in inverter-fed linear induction motor drive for reliability enhancement," *IEEE Trans. Ind. Electron.*, vol. 62, no. 7, pp. 4065–4077, Jul. 2015.

[19] H. Ro, D. Kim, H. Jeong, and K. Lee, "Tolerant control for power transistor faults in switched reluctance motor drives," *IEEE Trans. Ind. Appl.*, vol. 51, no. 4, pp. 3187–3197, Jul./Aug. 2015.

[20] P. Garg, S. Essakiappan, H. S. Krishnamoorthy, and P. N. Enjeti, "A fault-tolerant three-phase adjustable speed drive topology with active common-mode voltage suppression," *IEEE Trans. Power Electron.*, vol. 30, no. 5, pp. 2828–2839, May 2015.

[21] R. A. Keswani, H. M. Suryawanshi, and M. S. Ballal, "Multi-resolution analysis for converter switch faults identification," *IET Power Electron.*, vol. 8, no. 5, pp. 783–792, May 2015.

[22] M. Shahbazi, E. Jamshidpour, P. Poure, S. Saadate, and M. Zolghadri, "Open and short-circuit switch fault diagnosis for non-isolated DC-DC converters using field programmable gate array," *IEEE Trans. Ind. Electron.*, vol. 60, no. 9, pp. 4136–4146, Sep. 2013.

[23] E. Ribeiro, A. J. M. Cardoso, and C. Boccaletti, "Fault-tolerant strategy for a photovoltaic DC-DC converter," *IEEE Trans. Power Electron.*, vol. 28, no. 6, pp. 3008–3018, Jun. 2013.

[24] S. Y. Kim, K. Nam, H. S. Song, and H. G. Kim, "Fault diagnosis of a ZVS DC-DC converter Based on DC link current pulse shapes," *IEEE Trans. Ind. Electron.*, vol. 55, no. 3, pp. 1491–1494, Mar. 2008.

[25] E. Jamshidpour, P. Poure, E. Gholipour, and S. Saadate, "Single-switch DC–DC converter with fault-tolerant capability under open- and short-circuit switch failures," *IEEE Trans. Power Electron.*, vol. 30, no. 5, pp. 2703–2712, May 2015.

[26] E. Jamshidpour, P. Poure, and S. Saadate, "Photovoltaic systems reliability improvement by real-time FPGA-based switch failure diagnosis and fault-tolerant DC-DC converter," *IEEE Trans. Ind. Electron.*, vol. 62, no. 11, pp. 7247–7255, Nov. 2015.

[27] Y. Chen, S. Nie, X. Pei, and Y. Kang, "State monitoring and fault diagnosis of the PWM converter using the magnetic field near the inductor components," in *Proc. IEEE Energy Convers. Congr. Expo.*, Sep. 2010, pp. 1901–1907.

[28] S. Nie, Y. Chen, X. Pei, and Y. Kang, "A DSP-based diagnostic system for DC-DC converter using the shape of voltage across the magnetic

components," in *Proc. IEEE Energy Convers. Congr. Expo.*, Sep. 2010, pp. 1908–1915.
[29] X. S. Pu, T. H. Nguyen, D. C. Lee, K. B. Lee, and J. M. Kim, "Fault diagnosis of DC-link capacitors in three-phase AC/DC PWM converters by online estimation of equivalent series resistance," *IEEE Trans. Ind. Electron.*, vol. 60, no. 9, pp. 4118–4127, Sep. 2013.
[30] M. A. Vogelsberger, T. Wiesinger, and H. Ertl, "Life-cycle monitoring and voltage-managing unit for DC-link electrolytic capacitors in PWM converters," *IEEE Trans. Power Electron.*, vol. 26, no. 2, pp. 493–503, Feb. 2011.
[31] A. M. R. Amaral and A. J. M. Cardoso, "A simple offline technique for evaluating the condition of aluminum-electrolytic-capacitors," *IEEE Trans. Ind. Electron.*, vol. 56, no. 8, pp. 3230–3237, Aug. 2009.
[32] K. M. Tsang and W. L. Chan, "Low-cost sensing of equivalent series resistance for electrolytic capacitors," *IET Power Electron.*, vol. 2, no. 5, pp. 555–562, Sep. 2009.
[33] M. L. Gasperi, "Life prediction modeling of bus capacitors in AC variable frequency drives," *IEEE Trans. Ind. Appl.*, vol. 41, no. 6, pp. 1430–1435, Nov./Dec. 2005.
[34] K. M. Tsang and W. L. Chan, "Simple method for measuring the equivalent series inductance and resistance of electrolytic capacitors," *IET Power Electron.*, vol. 3, no. 4, pp. 465–471, Jul. 2010.
[35] A. M. R. Amaral and A. J. M. Cardoso, "Simple experimental techniques to characterize capacitors in a wide range of frequencies and temperatures," *IEEE Trans. Instrum. Meas.*, vol. 59, no. 5, pp. 1258–1267, May 2010.
[36] K. Harada, A. Katsuki, and M. Fujiwara, "Use of ESR for deterioration diagnosis of electrolytic capacitor," *IEEE Trans. Power Electron.*, vol. 8, no. 4, pp. 355–361, Oct. 1993.
[37] K. Yao, W. Tang, W. Hu, and J. Lyu, "A current-sensorless online ESR and C identification method for output capacitor of buck converter," *IEEE Trans. Power Electron.*, vol. 30, no. 12, pp. 6993–7005, Dec. 2015.
[38] T. H. Nguyen and D.-C. Lee, "Deterioration monitoring of DC-link capacitors in AC machine drives by current injection," *IEEE Trans. Power Electron.*, vol. 30, no. 3, pp. 1126–1130, Mar. 2015.
[39] M. Rigamonti, P. Baraldi, E. Zio, D. Astigarraga, and A. Galarza, "Particle filter-based prognostics for an electrolytic capacitor working in variable operating conditions," *IEEE Trans. Power Electron.*, vol. 31, no. 2, pp. 1567–1575, Feb. 2016.
[40] Z. S. Zhang, D. M. Xiao, and Y. Li, "Rogowski air coil sensor technique for on-line partial discharge measurement of power cables," *IET Sci. Meas. Tech.*, vol. 3, no. 3, pp. 187–196, May 2009.
[41] I. A. Metwally, "Performance improvement of slow-wave Rogowski coils for high impulse current measurement," *IEEE Sensors J.*, vol. 13, no. 2, pp. 538–547, Feb. 2013.
[42] T. Ghanbari and A. Farjah, "A magnetic leakage flux-based approach for fault diagnosis in electrical machines," *IEEE Sensors J.*, vol. 14, no. 9, pp. 2981–2988, Sep. 2014.
[43] M. Chiampi, G. Crotti, and A. Morando, "Evaluation of flexible Rogowski coil performances in power frequency applications," *IEEE Trans. Instrum. Meas.*, vol. 60, no. 3, pp. 854–862, Mar. 2011.
[44] O. Poncelas, J. A. Rosero, J. Cusido, J. A. Ortega, and L. Romeral, "Motor fault detection using a Rogowski sensor without an integrator," *IEEE Trans. Ind. Electron.*, vol. 56, no. 10, pp. 4062–4070, Oct. 2009.
[45] Y. Li, Y. Guo, Y. Long, C. Yao, Y. Mi, and J. Wu, "Novel lightning current sensor based on printed circuit board Rogowski coil," in *Proc. Int. Conf. High Voltage Eng. Appl.*, Sep. 2012, pp. 334–338.
[46] M. Shafiq, L. Kutt, M. Lehtonen, T. Nieminen, and M. Hashmi, "Parameters identification and modeling of high-frequency current transducer for partial discharge measurements," *IEEE Sensors J.*, vol. 13, no. 3, pp. 1081–1091, Mar. 2013.
[47] M. N. O. Sadiku, *Elements of Electromagnetics*, 6th ed. New York, NY, USA: Oxford Univ. Press, 2001.
[48] D. W. Hart, *Power Electronics*, New York, NY, USA: McGraw-Hill, 2010.

Ebrahim Farjah (M'12) received the B.Sc. degree in electrical and electronics engineering from Shiraz University, Shiraz, Iran, in 1987, the M.Sc. degree in electrical power engineering from the Sharif University of Technology, Tehran, Iran, in 1989, and the Ph.D. degree in electrical engineering from the Grenoble Institute of Technology, Grenoble, France.

He is currently a Professor at the Department of Electrical and Computer Engineering, Shiraz University. His research interests include power electronics, renewable energy, microgrids, and power quality.

Hadi Givi (S'15) received the B.Sc. degree in electrical power engineering from the Isfahan University of Technology, Isfahan, Iran, in 2010, and the M.Sc. degree in electrical power engineering from the Amirkabir University of Technology, Tehran, Iran, in 2012. He is currently working toward the Ph.D. degree in electrical power engineering at Shiraz University, Shiraz, Iran.

His main research interests include fault diagnosis in power electronic converters and analyzing electromagnetic systems using FEM.

Teymoor Ghanbari received the B.Sc. degree in Electrical Power Engineering from S.R. University, Tehran, Iran, in 1997, the M.Sc. degree from Shahrood University of Technology, Shahrood, Iran, in 2007, and the Ph.D. degree in electrical power engineering from Shiraz University, Shiraz, Iran, in 2012.

He is currently an Assistant Professor at the School of Advanced Technologies, Shiraz University. His research interests include distributed generation, power electronics, and electrical machines.